

Analysis and Design of Microring-Based Switching Elements in a Silicon Photonic Integrated Transponder Aggregator

Paolo Pintus, *Member, IEEE*, Pietro Contu, Nicola Andriolli, Antonio D'Errico, Fabrizio Di Pasquale, *Member, IEEE*, and Francesco Testa

Abstract—In this paper, we present and investigate a new architecture of a silicon photonic transponder aggregator as a new interconnect subsystem enabling the implementation of colorless, directionless, and contentionless ROADMs. Such subsystem is based on a microring resonator switching fabric integrated in a silicon photonics platform to achieve high functional integration together with reduction of cost, footprint, and power consumption. In the proposed device, microring resonators perform simultaneous add and drop of wavelength channels which suffer from two detrimental effects: residual dropped signal crosstalk and residual added signal crosstalk, respectively. Considering three microring-based switching elements, the transfer matrix method has been used to compute the add/drop transfer functions of the switches as a function of their geometrical parameters. The two crosstalk effects have been evaluated jointly with other important transmission parameters, such as bandwidth, insertion losses, side lobe suppression, adjacent channel rejection, extinction ratio, and group dispersion. In addition, device sensitivity with respect to the ring-waveguide coupling coefficients has been calculated. Finally, the performance of the different switches has been assessed to demonstrate that, by a proper design, the proposed transponder aggregator can support 100 Gb/s DP-QPSK modulated signal transmission.

Index Terms—Integrated optics, optical switches, ring resonators.

I. INTRODUCTION

DYNAMIC rearrangement of capacity while optimizing transport resources utilization and further lowering capital cost and power consumption is a fundamental requirement for next generation optical transport networks. These features can be ensured by implementing highly flexible transport nodes in conjunction with an intelligent control and management plane empowering software defined networking (SDN) [1].

Conventional reconfigurable optical add and drop multiplexer (ROADM) nodes are implemented using broadcast-and-select architecture. Fig. 1 shows a four-directional ROADM based on

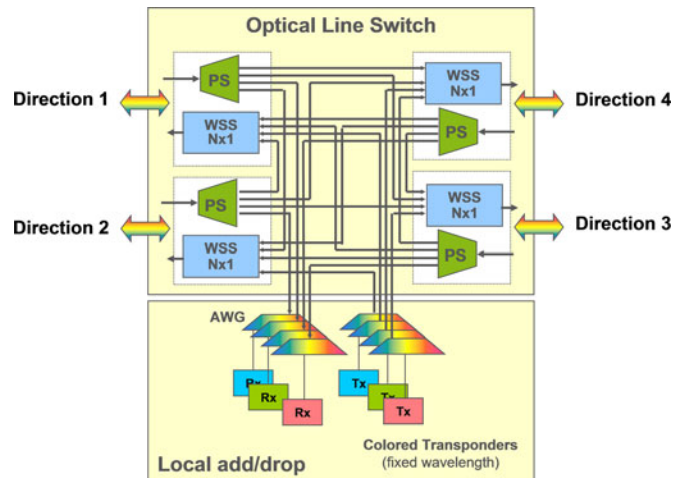


Fig. 1. Conventional ROADM architecture.

two main system blocks: the optical line switching section and the local add and drop section. The former comprises, for each direction, a $N \times 1$ (with N equal to the node directions) wavelength selective switching (WSS) module to selectively combine onto the output fiber the wavelengths distributed by the different power splitters (PS). Local add and drop section includes arrayed waveguide gratings (AWG) to interconnect the optical line switch to fixed wavelength transponders (Tx modules in Fig. 1). For signal dropping, an array of AWG demultiplexers is used to separate the signals distributed by the power splitter in each network direction before reception at the receivers (Rx modules). Similarly, another AWG array is used to multiplex the locally generated signals to be added to each network direction. In such conventional nodes, full switching flexibility is only ensured for wavelength channels in transit across the node toward other nodes. Actually these channels can be routed from any to any direction. On the contrary, added and dropped wavelengths are rigidly assigned to a fixed direction and to a fixed color (by means of WDM multiplexer and demultiplexer array) and any change in these configurations must be performed by manual rewiring [2].

Next generation ROADM should provide higher flexibility with respect to currently deployed optical nodes. In such new nodes, the routing of added/dropped wavelength channels to/from any direction should be guaranteed without any manual intervention (directionless operation), independently from the transponder wavelength (colorless operation) and by allowing

Manuscript received June 14, 2013; revised July 31, 2013; accepted August 1, 2013. Date of publication August 5, 2013; date of current version November 27, 2013.

P. Pintus, P. Contu, N. Andriolli, and F. Di Pasquale are with the Scuola Superiore Sant'Anna, 56124 Pisa, Italy (e-mail: paolo.pintus@sssup.it; pietro.contu@sssup.it; nick@sssup.it; f.dipasquale@sssup.it).

A. D'Errico and F. Testa are with the Ericsson S.p.A, 56124 Pisa, Italy (e-mail: antonio.d.ericco@ericsson.com; francesco.testa@ericsson.com).

Color versions of one or more of the figures in this paper are available online at <http://ieeexplore.ieee.org>.

Digital Object Identifier 10.1109/JLT.2013.2276852

multiple transponders operating at the same wavelength to be handled by the same add and drop section (contentionless operation) [3], [4]. In order to address these new requirements without significantly increasing cost, footprint, and complexity, photonic integrated devices will play a crucial role. The architecture of a new silicon photonic system on chip (SoC) is presented and investigated.

The paper is organized as follows: in Section II, the concept of a colorless directionless contentionless (CDC) ROADM is introduced and a new integrated device as transponder aggregator (TPA) is presented and discussed in Section III. The proposed TPA architecture is based on a switching fabric, which can be performed using silicon microring resonators on a silicon-on-insulator (SOI) platform. In this study, three switching elements are investigated, which are presented in Section IV. A rigorous mathematical model of such switches is introduced in Section V, followed by the simulation results, which are illustrated in Section VI. By considering the relevant features of a ring-based switching element (i.e., the full width at half maximum bandwidth, the insertion losses, the side lobe suppression, the adjacent channel rejection, the extinction ratio, and the group dispersion), we have shown that only one of the three switch configurations meets all the identified requirements. This switch is made up of two waveguides, crossing at an angle θ , and two rings located on the opposite side of the waveguide crossing. Optimizing the ring-waveguide coupling coefficient and the angle θ , we verified that such a switching element can support high speed transmission. The TPA performance is eventually discussed in Section VII and in Section VIII, the conclusions are drawn.

II. CDC ROADM NODES

The colorless, directionless and contentionless operations in the ROADM nodes (CDC ROADM) will give the possibility to optimize the resource utilization, to reconfigure network according to the variation of traffic pattern in a cost effective way, also supporting rerouting functions in case of faults. In fully flexible CDC ROADMs, WSS devices will continue to be used in the optical line switching section, while a new architecture of the local add/drop section has to be considered as illustrated in Fig. 2. It is worth noting that in Fig. 2, the PS in the optical line switch section have been replaced by WSS only in order to improve the node isolation and ease transponder scalability. In the new add and drop section, alternative blocks replace AWG blocks [5]. These blocks are included in a new equipment presented in this paper as TPA. For the add (drop) function the TPA selects the direction to which the transponder wavelength has to be added (dropped) and combines it together with the wavelengths to be added (dropped) to the same direction from other transponders. To compensate for the TPA loss, an array of N optical amplifiers (not shown in Fig. 2) is required at the interface of the TPA to the optical line switch.

The function of the TPA is to add the required flexibility at the end point, between the line switching subsystem and the transponder subsystem.

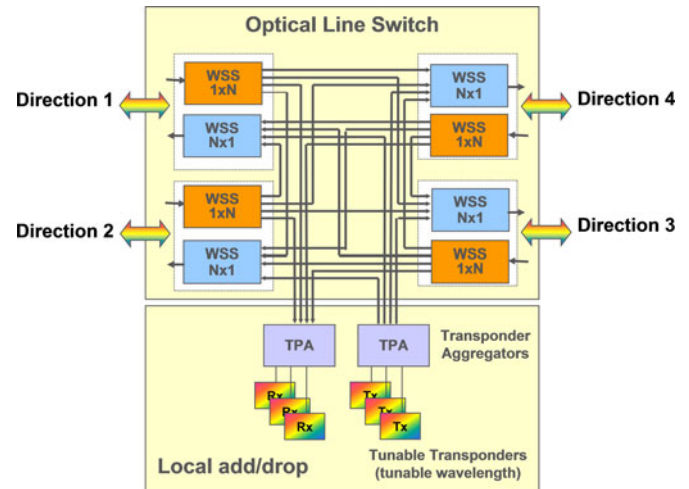


Fig. 2. CDC ROADM architecture.

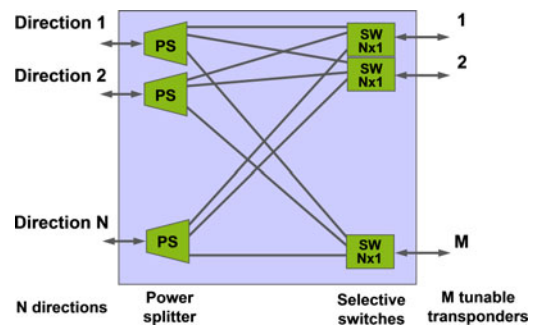


Fig. 3. TPA block diagram.

An implementation of a TPA, schematically shown in Fig. 3, mainly consists of an $N \times M$ optical switching matrix with N ports connected to the line switching subsystem (typically four or eight) and M ports connected to the transponders (typically 12 or 16). For the drop functions, the sets of wavelengths that need to be dropped are sent from each direction to the TPA using the WSS devices. Within the TPA, the different sets of wavelengths are first distributed by means of power splitters (PS) and then $N \times 1$ switches (SW) are employed to select the set of wavelengths to be sent to the transponders. A single channel from this comb is then selected by tunable filters placed in front of the transponder. Another TPA, with the same internal structure, provides the add functions. For this purpose, tunable lasers are used without requiring tunable filters. The proposed architecture scales easily with the number of transponders by connecting an additional TPA to the spare ports of the WSS.

Such architecture for the TPA has been developed and presented in [6], where planar lightwave circuits (PLC) technology has been used. More recently, silicon photonic integrated TPA devices have been realized integrating on the same chip a matrix of Mach-Zehnder based 2×2 switching elements and a cyclic 8×8 AWG [7]. Silicon photonic integration provides an attractive technology due to its potential of implementing photonic switching devices with unprecedented low cost and small footprint characteristics.

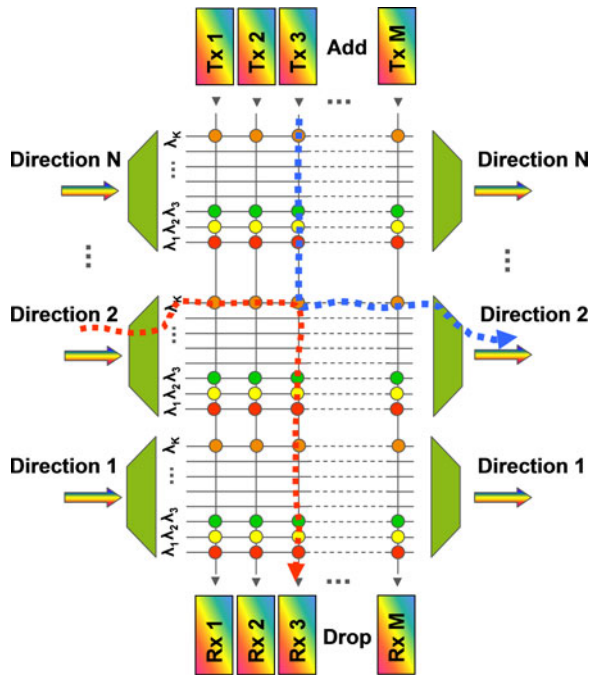


Fig. 4. Conceptual TPA block diagram.

III. SILICON PHOTONICS INTEGRATED TPA

The SoC TPA proposed in this paper is based on silicon photonics technology and uses a scalable matrix of color-coded microring resonator switching elements in conjunction with WDM multiplexers and demultiplexers. The conceptual architecture of the TPA is shown in Fig. 4. According to this architecture, a single switching matrix is used for both add and drop functions. The matrix has dimension $NK \times M$, where N is the number of fibers (i.e., $N = 4$), K is the number of wavelengths per fiber (i.e., $K = 48$), and M is the number of ports connected to transponders (i.e., $M = 12$). The matrix is placed between AWG multiplexer and demultiplexer elements.

Tunable transmitters are connected at the top of the matrix and the wavelength channels to be added proceed vertically along one column crossing many switching elements until they are eventually horizontally switched. The switching occurs at the elementary switch corresponding to the color of the signal and to the direction to which it must be added. The signal eventually arrives at the input of the wavelength multiplexer.

For the drop function, the wavelengths to be dropped pass through a wavelength demultiplexer, and then, proceed horizontally along the color-coded rows until they are vertically switched by the switching elements in the column of the selected receivers. They proceed vertically across many switching elements until they arrive to the receivers connected at the bottom of the switching matrix as shown in Fig. 4.

Fig. 4 reports an example where the dotted blue line represents a wavelength to be added to direction 2 by the transponder Tx 3, working at color λ_K , and simultaneously, a signal at the same color λ_K (represented by the dotted red line) must be dropped from the same direction 2 at the transponder Rx 3. This example points out that the TPA can perform simultaneously both add

and drop operations by activating the same switching element. As a matter of fact, the same switching element, driven to switch horizontally a given added channel coming from the top, is able to switch vertically the same wavelength that comes from the left.

It is worth noting that only M (e.g., 12 or 16) channels are injected in the TPA by the N input directions. Indeed, the WSSs select only the channels that must be added/dropped, which are at maximum equal to the number of transponders. Let us also observe that for this goal just one switch in each column needs to be locked, while the rest of the rings are simply put out of band to let the signal pass transparently.

To perform the control of the switching elements in closed loop, integrated photodetectors can be located at the drop ports. Thermal heaters can be effectively used to trim the resonance of the rings [8], allowing to switch ON (i.e., ring resonance aligned with the selected channel) and OFF (i.e., ring resonance shifted with respect to the channels) the switching elements. Designing properly the location and the size of the heaters as well as the spacing and the configuration of the rings, allows to strongly minimize the thermal crosstalk amongst the switches, which is defined as the phase change ratio induced by the closest ring-based switch due to the heated switch. It has been proved that a distance larger than $15\mu\text{m}$ and thermal isolation trenches can successfully reduce the thermal crosstalk [9]. Moreover, in our device all the crosspoint switches are uniquely designed for their particular wavelength and the rings need just a small heat to be switched ON/OFF and to be trimmed in order to compensate the fabrication errors. As a result, the variation of the temperature across the chip will be limited as well as the thermal crosstalk.

As it is well known, due to material stress and waveguide geometry, polarization birefringence occurs in silicon planar waveguide components. In order to preserve polarization information, polarization diversity configuration must be designed. For this reason, polarization splitters and rotators must be considered at the input/output of the device.

IV. MICRORING-BASED SWITCHING ELEMENTS

To implement such an integrated TPA, different microring switching element configurations can be considered, each characterized by different performances. The most relevant ones are shown in Fig. 5.

The simplest ring-based switching element is constituted by a single microring placed on one corner of the waveguide crossing as shown in Fig. 5(a) [10]. Let IN and OUT be the input and the output direction of the network, while Add and $Drop$ are the local ports for adding/dropping a single channel to/from transponders. When a WDM signal is propagating from IN to OUT and the resonance wavelength of the ring matches a wavelength carrier, that channel can be dropped to the $Drop$ port and replaced by a new one coming from the Add port. It is worth noting that the add/drop functions work simultaneously at the same wavelength. For this reason, we have introduced and investigated two new important parameters defined as the *residual dropped signal crosstalk* ($C_{R.D.}$) and the *residual added signal crosstalk* ($C_{R.A.}$). The $C_{R.D.}$ is measured at the OUT port and

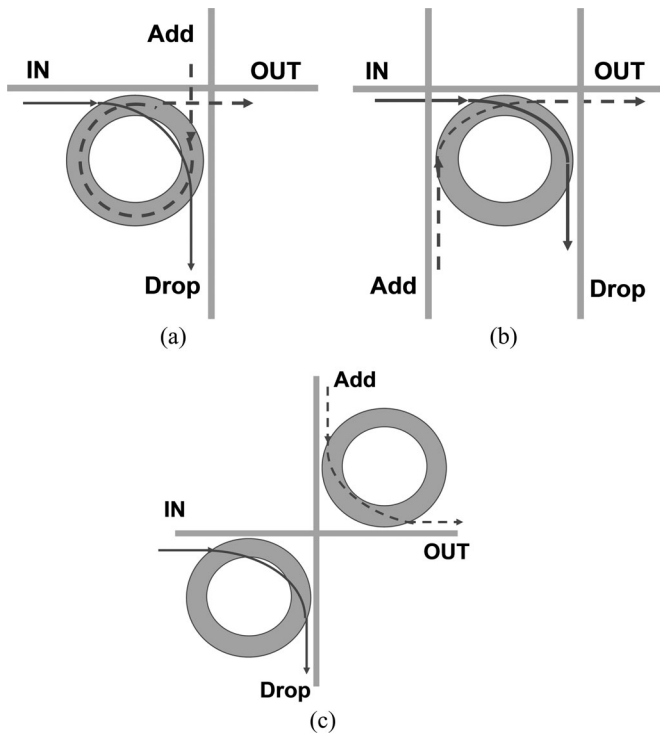


Fig. 5. Three microring configurations under investigation. (a) Two-waveguide add/drop switch with a single ring. (b) Three-waveguide add/drop switch with a single ring. (c) Two-waveguide add/drop switch with two rings.

is defined as the ratio between the remaining part of the dropped signal and the added signal. Vice versa, the $C_{R.A.}$ is the ratio between the remaining part of the added signal and the dropped signal at the *Drop* port. Let us note that when a new signal is injected from the *Add* port, it is expected to be completely sent to the *OUT* port; however, it is also partially coupled to the *Drop* port. For the switching element in Fig. 5(a), the interference between the added signal and the dropped signal at *Drop* port might be very high because the add and drop ports are on the opposite ends of the same waveguide. Note that while the dropped signal is usually quite low in terms of power because coming from the network (e.g., -15 dBm or lower), the added signal might be much larger because it has just been generated by a tunable transponder (e.g., 5 dBm or even higher). Due to this fact, the two signals are quite unbalanced in terms of power and a $C_{R.A.}$ smaller than -40 dB is then needed. It is worth to note that those two crosstalk effects are the contributor of the coherent (same wavelength) crosstalk.

A slightly modified version of the aforementioned configuration is depicted Fig. 5(b), where a single ring is placed between two waveguide crossings, and add/drop ports are placed at the end of two separated waveguides in order to minimize the issues of the former switching element.

Alternatively, we can add another ring to the switch in Fig. 5(a). The new switching element is shown in Fig. 5(c), where two resonators are placed on the opposite corners of the waveguide crossing [11]. Note that while the first ring mainly performs the drop function, the second one is mostly responsible of the adding. Concerning this structure, in this study, we

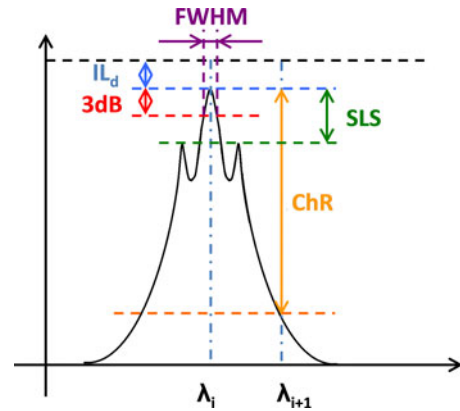


Fig. 6. Relevant features of a ring-based switch: full-width at half-maximum bandwidth (FWHM), the insertion loss (IL), the side lobe suppression (SLS), and the adjacent channel rejection (ChR).

have introduced an extra degree of freedom by varying the angle between the two waveguides. The result of using two rings is to enlarge the coupling, and consequently, to decrease the crosstalk.

Let us note that the switching element in Fig. 5(a) can be seen as a special case of the one shown in Fig. 5(c), when the second ring has been removed or it is not coupled to the two waveguides. As a consequence, in the following, we will focus on the mathematical model of the second and third switches, because the first structure can be easily derived.

In addition to the two previously defined crosstalk effects, the performance of the ring-based switches has been evaluated also in terms of the full-width at half-maximum bandwidth (FWHM), the drop insertion loss (IL_d), the side lobe suppression (SLS), and the adjacent channel rejection (ChR), which are schematically shown in Fig. 6. Let us also note that the side lobes do not appear when a single ring is used.

The ChR is a quite important parameter to evaluate the performance of the device in WDM applications. In this paper, the ChR has been evaluated considering a channel spacing of 100 GHz, however larger channel spacing (i.e., 200 GHz) will produce higher rejection.

Varying the refractive index by thermal heating, the ring resonance can be shifted, switching ON and OFF the corresponding crosspoint. To evaluate the performance of the switching between the two states, two parameters have been considered: the extinction ratio (ER) and the bypass insertion loss (IL_{bp}). The former is defined as the ratio of the optical power between the ON and OFF states, while the latter is the loss when the ring is out of resonance (OFF state), both shown in Fig. 7(a) and (b), respectively. For the sake of clarity, in the plots of Fig. 7, we have not considered the side lobes.

A high value of ER is fundamental to reduce the incoherent crosstalk, which is the sum of the contribution of all the intervening channels. To explain its importance, let us recall that only one ring is resonating in each vertical path, while the others are out of resonance. If they are not switched OFF completely, part of the other channels, which are propagating horizontally, can be partially dropped resulting in an incoherent noise on

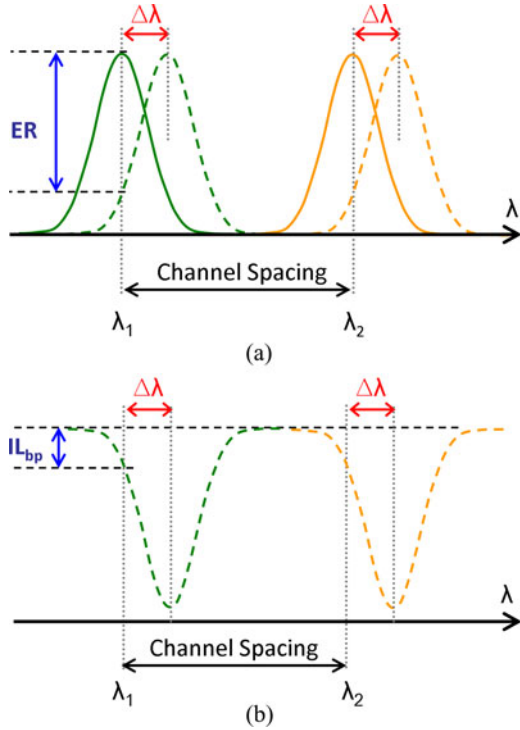


Fig. 7. Extinction ratio (ER) and Bypass Insertion Loss (IL_{bp}) for a ring-based switch in an OFF state. (a) Drop function. (b) Through function.

the wanted signal. Assuming a uniform ER and M channels, the incoherent total power from the intervening channels will be $10 \log_{10}(M - 1)$ dB higher. In our case, for $M = 12$, that value is about 11 dB. To guarantee a small incoherent crosstalk, an ER higher than 35 dB is then needed. However, this constraint can be relaxed by filtering out all the incoherent noise with an integrated tunable filter, as a result lower ER are permitted. Vice versa, a low IL_{bp} allows a signal to pass through the switch without been attenuated. To complete our analysis, we will also explore the dispersion induced by the drop and through transfer functions.

In the following, we will investigate and optimize the switching elements in terms of the ring-waveguide coupling coefficients and also in terms of the angle θ for the two-ring configuration.

Ring-waveguide couplers and waveguide crossings may affect the network performance introducing loss, crosstalk, and bandwidth limitation [12]. Vice versa, waveguide propagation loss is usually sufficiently low to support global interconnection on the chip due to the small size of the device. In this study, we will focus our attention on the influence of ring-waveguide coupling, while we assume that the effect of waveguide crossings is negligible. This choice is supported by the fact that compact structures like mode-field expanders can guarantee a crosstalk lower than -45 dB in a broad wavelength range [13], [14]. For each waveguide crossing, an insertion loss as low as 0.16 dB has been reported, which might not be negligible after a cascade of several crossings. That loss can be effectively compensated by using integrated hybrid semiconductor optical amplifiers within the TPA [15], [16].

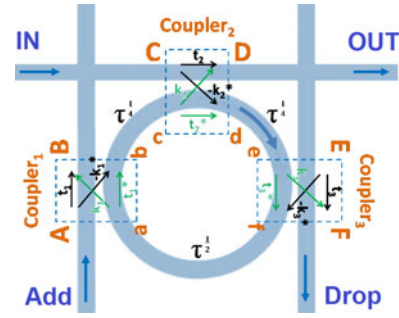


Fig. 8. Top-view of the three-waveguide add/drop switch.

Evaluating the previous configurations, we show that only the two-waveguide switch with two rings satisfies the design constraint for our TPA application.

V. MATHEMATICAL MODEL

The transfer function of the devices is computed using the transfer matrix method [17], [18]. Assuming lossless couplers, the field cross-coupling coefficient and the field transmission coefficient at the ring-waveguide coupling area are $k = j\sqrt{K}$ and $t = \sqrt{1 - K}$, respectively, where K is the ring-waveguide power coupling ratio. The code has been also validated with the results shown in [18].

In this study, we have considered $420 \text{ nm} \times 220 \text{ nm}$ TE single-mode silicon waveguides, manufactured on a SOI platform. In our analysis, β_{wg} and α_{wg} are the waveguide phase and attenuation constants, whereas β_{rr} and α_{rr} are the phase and the attenuation constants for the ring, respectively. The phase constants $\beta_{wg/rr}$ have been computed using a full-vectorial finite-element solver [19], [20], while the attenuation values $\alpha_{wg/rr}$ have been taken from the literature [21].

Assuming R the ring radius, let us also introduce $\tau = \exp[-(\alpha_{rr} - j\beta_{rr})2\pi R]$ as the ring round-trip transmission factor. Its amplitude is related to the ring-loss ($|\tau| = 1$ means lossless resonator) and its phase is the ring round-trip phase change. For example, the term $\tau^{1/4}$ represents the field component that propagates along a quarter of the ring.

A. Three-Waveguide Switch

Referring to Fig. 8, we use the capital letters for the signals propagating in the waveguides and the lower case for the corresponding waves in the ring. Let (A, C, E) be the ingoing waves to *Coupler*₁, *Coupler*₂ and *Coupler*₃, respectively, while the outgoing signals are (B, D, F) . The corresponding ingoing-coupler and outgoing-coupler waves in the ring are (a, c, e) and (b, d, f) , respectively. Using the relations in [17], we have

$$\begin{pmatrix} B \\ b \end{pmatrix} = \begin{pmatrix} t_1 & k_1 \\ -k_1^* & t_1^* \end{pmatrix} \begin{pmatrix} A \\ a \end{pmatrix}, \quad \begin{pmatrix} D \\ d \end{pmatrix} = \begin{pmatrix} t_2 & k_2 \\ -k_2^* & t_2^* \end{pmatrix} \begin{pmatrix} C \\ c \end{pmatrix}$$

$$\begin{pmatrix} F \\ f \end{pmatrix} = \begin{pmatrix} t_3 & k_3 \\ -k_3^* & t_3^* \end{pmatrix} \begin{pmatrix} E \\ e \end{pmatrix}. \quad (1)$$

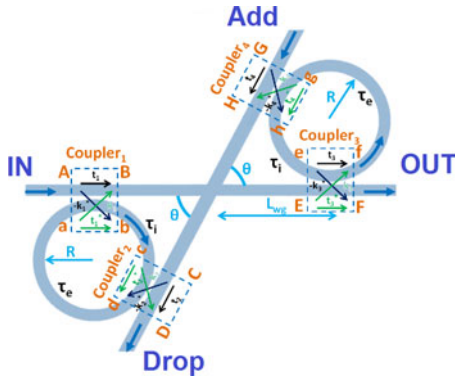


Fig. 9. Top-view of the two-waveguide add/drop switch.

Additionally, the waves in the ring are related by the following phase-shift relations

$$c = \tau^{1/4}b, \quad e = \tau^{1/4}d, \quad a = \tau^{1/2}f. \quad (2)$$

After some algebraic manipulations, it can be shown that (B, D, F) are linked to (A, C, E) by the following linear relations:

$$\begin{pmatrix} B \\ D \\ F \end{pmatrix} = \begin{pmatrix} T_{11} & T_{12} & T_{13} \\ T_{21} & T_{22} & T_{23} \\ T_{31} & T_{32} & T_{33} \end{pmatrix} \begin{pmatrix} A \\ C \\ E \end{pmatrix} \quad (3)$$

where

$$T_{11} = \frac{t_1 - t_2^*t_3(|t_1|^2 + |k_1|^2)\tau}{1 - t_1^*t_2^*t_3^*\tau} \quad (4a)$$

$$T_{22} = \frac{t_2 - t_1^*t_3(|t_2|^2 + |k_2|^2)\tau}{1 - t_1^*t_2^*t_3^*\tau} \quad (4b)$$

$$T_{33} = \frac{t_3 - t_1^*t_2(|t_3|^2 + |k_3|^2)\tau}{1 - t_1^*t_2^*t_3^*\tau} \quad (4c)$$

$$T_{12} = -\frac{k_1k_2^*t_3^3\tau^{3/4}}{1 - t_1^*t_2^*t_3^*\tau}, \quad T_{13} = -\frac{k_1k_3^*\tau^{1/2}}{1 - t_1^*t_2^*t_3^*\tau} \quad (4d)$$

$$T_{23} = -\frac{t_1^*k_2k_3^*\tau^{3/4}}{1 - t_1^*t_2^*t_3^*\tau}, \quad T_{21} = -\frac{k_1^*k_2\tau^{1/4}}{1 - t_1^*t_2^*t_3^*\tau} \quad (4e)$$

$$T_{31} = -\frac{k_1^*t_2^*k_3\tau^{1/2}}{1 - t_1^*t_2^*t_3^*\tau}, \quad T_{32} = -\frac{k_2^*k_3\tau^{1/4}}{1 - t_1^*t_2^*t_3^*\tau}. \quad (4f)$$

Let us note that the previous equations hold also in the case of lossy couplers, i.e., with $(|t_i|^2 + |k_i|^2) < 1$ for $i = 1, 2, 3$.

B. Two-Waveguide Switch

Exploiting the same approach used for the three-waveguide switch, we can compute the transfer matrix for the second structure reported in Fig. 9.

Considering the directions shown in Fig. 9, the inputs are labeled with *IN* and *Add*, while the outputs are *OUT* and *Drop*. Using the notation reported in the figure, we have $A = IN$, $G = Add$, $F = OUT$ and $D = Drop$.

Relating the input to the output waves at each coupler, we get

$$\begin{pmatrix} B \\ b \end{pmatrix} = \begin{pmatrix} t_1 & k_1 \\ -k_1^* & t_1^* \end{pmatrix} \begin{pmatrix} A \\ a \end{pmatrix}, \quad \begin{pmatrix} D \\ d \end{pmatrix} = \begin{pmatrix} t_2 & k_2 \\ -k_2^* & t_2^* \end{pmatrix} \begin{pmatrix} C \\ c \end{pmatrix} \quad (5a)$$

$$\begin{pmatrix} F \\ f \end{pmatrix} = \begin{pmatrix} t_3 & k_3 \\ -k_3^* & t_3^* \end{pmatrix} \begin{pmatrix} E \\ e \end{pmatrix}, \quad \begin{pmatrix} H \\ h \end{pmatrix} = \begin{pmatrix} t_4 & k_4 \\ -k_4^* & t_4^* \end{pmatrix} \begin{pmatrix} G \\ g \end{pmatrix} \quad (5b)$$

where (5a) and (5b) refer to the first and second ring in Fig. 9, respectively. As we did in the previous case, we have to take into account the phase-shift relations

$$c = \tau_i b, \quad a = \tau_e d, \quad g = \tau_e f, \quad e = \tau_i h \quad (6)$$

where $\tau_{i/e} = \tau^{\frac{1}{2}(1 \mp \frac{\theta}{\pi})}$. In this case, we must also consider the phase delay between the two rings, which means

$$E = pB, \quad C = pH. \quad (7)$$

This extra phase shift parameter $p = e^{-2(\alpha_{wg} - j\beta_{wg})L_{wg}}$ is related to the distance between the rings $2L_{wg} \simeq 2R/\tan(\theta/2)$. It can be easily shown that (F, D) are related to (A, G) by the following linear relations:

$$\begin{pmatrix} F \\ D \end{pmatrix} = \begin{pmatrix} R_1 & T_1 \\ T_2 & R_2 \end{pmatrix} \begin{pmatrix} A \\ G \end{pmatrix} \quad (8)$$

where

$$R_1 = \frac{\alpha_1\alpha_3}{1 - \beta_1\beta_4}, \quad T_1 = -\left(\beta_3 + \frac{\beta_1\alpha_3\alpha_4}{1 - \beta_1\beta_4}\right) \quad (9a)$$

$$R_2 = \frac{\alpha_2\alpha_4}{1 - \beta_1\beta_4}, \quad T_2 = -\left(\beta_2 + \frac{\alpha_1\alpha_2\beta_4}{1 - \beta_1\beta_4}\right) \quad (9b)$$

and

$$\alpha_1 = \frac{t_1 - t_2^*(|t_1|^2 + |k_1|^2)\tau}{1 - t_1^*t_2^*\tau}, \quad \beta_1 = \frac{k_1k_2^*p\tau_e}{1 - t_1^*t_2^*\tau} \quad (10a)$$

$$\alpha_2 = \frac{t_2p - t_1^*(|t_2|^2 + |k_2|^2)p\tau}{1 - t_1^*t_2^*\tau}, \quad \beta_2 = \frac{k_1^*k_2\tau_i}{1 - t_1^*t_2^*\tau} \quad (10b)$$

$$\alpha_3 = \frac{t_3p - t_4^*(|t_3|^2 + |k_3|^2)p\tau}{1 - t_3^*t_4^*\tau}, \quad \beta_3 = \frac{k_3k_4^*\tau_i}{1 - t_3^*t_4^*\tau} \quad (10c)$$

$$\alpha_4 = \frac{t_4 - t_3^*(|t_4|^2 + |k_4|^2)\tau}{1 - t_3^*t_4^*\tau}, \quad \beta_4 = \frac{k_3^*k_4p\tau_e}{1 - t_3^*t_4^*\tau}. \quad (10d)$$

Like in the previous case, the (10a)–(10d) are also valid in the case of lossy couplers, i.e., $(|t_i|^2 + |k_i|^2) < 1$ for $i = 1, 2, 3, 4$. Note that the transfer function for the switching element shown in Fig. 5(a) can be easily computed assuming $k_3 = k_4 = 0$, $t_3 = t_4 = 1$, and $\theta = 90^\circ$.

When the signal is injected only from *IN* (i.e., $A = 1$, $G = 0$), the output signals F (*OUT*) and D (*Drop*) are given by the reflection and transmission coefficients R_1 and T_2 , respectively. Vice versa, when the signal is injected only from the *Add*-port (i.e., $A = 0$, $G = 1$), the output signals F (*OUT*) and D (*Drop*) are given by the transmission and reflection coefficients T_1 and R_2 , respectively.

Let us observe that in this switch configuration (see Fig. 9), we can identify two closed-loop paths: the light can resonate in the rings and in the loop made of the two waveguide segments and the external part of the two rings. This second loop has a figure-eight shape with two lobes. More precisely, let us define the optical phase difference in the ring $(\Delta\phi)_{rr}$ as the phase shift after one ring round trip, and let $(\Delta\phi)_{wg}$ be the phase shift after one trip through the waveguides and the ring resonators. Note that the phase difference $(\Delta\phi)_{rr}$ corresponds to the phase of the ring round-trip transmission factor τ , previously introduced. As a result, we have

$$\begin{aligned} (\Delta\phi)_{wg} &= 2\beta_{wg}(2L_{wg}) + 2\angle\tau_e \\ &= 4\beta_{wg} \frac{R}{\tan(\frac{\theta}{2})} + 4\pi R\beta_{rr} \left(\frac{\pi + \theta}{2\pi} \right) \end{aligned} \quad (11a)$$

$$(\Delta\phi)_{rr} = \beta_{rr}2\pi R. \quad (11b)$$

If $(\Delta\phi)_{wg}/2\pi = m_1$ and $m_1 = 1, 2, \dots$, then figure-eight loop is resonating, vice versa when $(\Delta\phi)_{wg}/(2\pi) = (1 + 2m_1)/2$ and $m_1 = 0, 1, \dots$, the same loop is completely out-of-resonance. Similarly, the rings are on resonance when $(\Delta\phi)_{rr}/2\pi = m_2$ and $m_2 = 1, 2, \dots$, while they are out-of-resonance, if $(\Delta\phi)_{wg}/(2\pi) = (1 + 2m_2)/2$ and $m_2 = 0, 1, \dots$. According to the previous conditions, we can have four possible situations:

- (α) resonance of both rings and figure-eight loop;
- (β) resonance of the rings and the figure-eight loop completely out-of-resonance;
- (γ) the rings completely out-of-resonance and the figure-eight loop resonating;
- (δ) both the rings and figure-eight loop completely out-of-resonance.

C. Crosstalk Parameters Calculation

For our applications, the signal power levels are such that the linear regime operating condition can be assumed for the silicon waveguides. By using the superposition principle, the $\mathbb{C}_{R,D.}$ and the $\mathbb{C}_{R,A.}$ can be computed for the three-waveguide switch configuration

$$\mathbb{C}_{R,D.} = \frac{D|_{A=0,C=1,E=0}}{D|_{A=1,C=0,E=0}} = \frac{|T_{22}|}{|T_{21}|} \quad (12a)$$

$$\mathbb{C}_{R,A.} = \frac{F|_{A=1,C=0,E=0}}{F|_{A=0,C=1,E=0}} = \frac{|T_{31}|}{|T_{32}|}. \quad (12b)$$

Similarly, the residual dropped and added signal crosstalks for the two-waveguide add/drop switching elements are, respectively,

$$\mathbb{C}_{R,D.} = \frac{F|_{A=1,G=0}}{F|_{A=0,G=1}} = \frac{|R_1|}{|T_1|} \quad (13a)$$

$$\mathbb{C}_{R,A.} = \frac{D|_{A=0,G=1}}{D|_{A=1,G=0}} = \frac{|R_2|}{|T_2|}. \quad (13b)$$

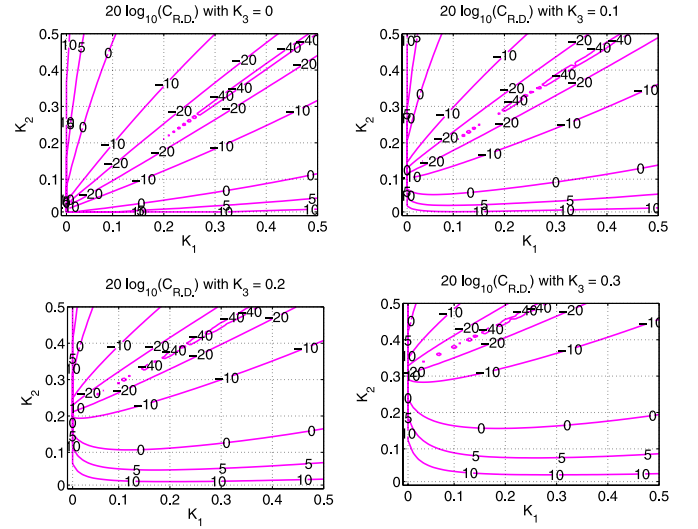


Fig. 10. Contour maps of the residual dropped signal crosstalk $\mathbb{C}_{R,D.}$ in dB on the (K_1, K_2) -plane with a fixed value of the coupling constant K_3 .

VI. NUMERICAL RESULTS

Using the model illustrated in Section V, we have numerically analyzed the behavior of the three switching elements presented in Section III. The performance of the ring-based switches have been investigated in terms of $\mathbb{C}_{R,D.}$, $\mathbb{C}_{R,A.}$, $FWHM$, SLS , IL_d , and ChR , by varying the coupling coefficients K_i .

All the simulations have been made by considering a ring radius $R = 10 \mu\text{m}$, corresponding to a loss coefficient $\alpha_{rr} = \frac{36 \text{ dB}}{\pi \text{ cm}}$ [21]. Smaller ring radii will introduce higher bending losses due to radiation. Concerning the silicon waveguides, we assumed $\alpha_{wg} = 2.7 \frac{\text{dB}}{\text{cm}}$ [21]. Because of the high confinement factor reached in silicon waveguide, the couplers have been assumed lossless (i.e., $|t_i|^2 + |k_i|^2 = 1$, $i = 1, 2, 3, 4$). Note that in order to have a more accurate model, we have considered the coefficient K_i of the i th coupler to be dependent on the wavelength λ as follows [22]:

$$K_i(\lambda) \propto \frac{1}{\lambda^2}. \quad (14)$$

A. Three-Waveguide Switch

Let us start our analysis from Fig. 10, which shows the contour plots of $20 \log_{10}(\mathbb{C}_{R,D.})$ for four different K_3 values ($K_3 = 0$, $K_3 = 0.1$, $K_3 = 0.2$, and $K_3 = 0.3$, respectively). It is worth noting that moving along the straight line $K_2 = (1 - K_3)|\tau|^2(K_1 - 1) + 1$, $\mathbb{C}_{R,D.}$ is minimal.

In Fig. 11, to preserve the symmetry, we assume $K_1 = K_3$. As a result, the residual dropped signal crosstalk $\mathbb{C}_{R,D.}$ takes the following form

$$\mathbb{C}_{R,D.} = \frac{\sqrt{1 - K_2} - (1 - K_1)|\tau|}{\sqrt{K_1 K_2} |\tau|^{\frac{1}{4}}} \quad (15)$$

and it goes to zero on the curve described by the following equation

$$K_1 = 1 - |\tau|^{-1} \sqrt{1 - K_2}. \quad (16)$$

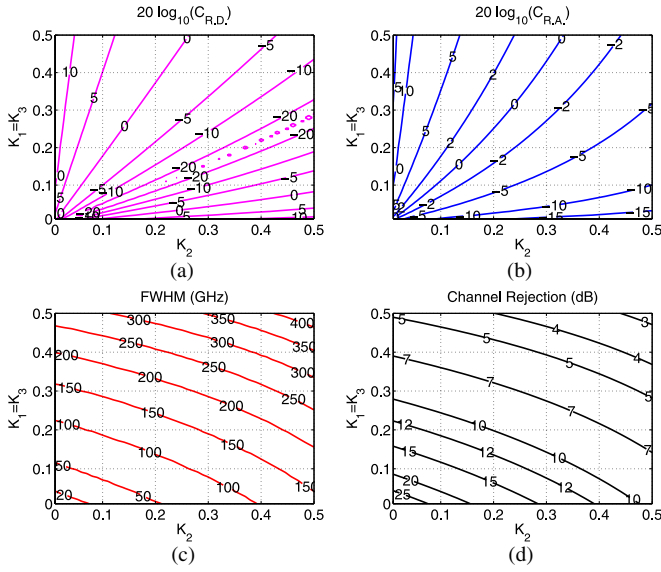


Fig. 11. (a) Contour plot of the residual dropped signal crosstalk $\mathcal{C}_{R,D}$, given in (15). (b) Contour plot of the residual added signal crosstalk $\mathcal{C}_{R,A}$. (c) Contour plot of $FWHM$ for the single-ring switch. (d) Contour plot of ChR in dB.

Therefore, the quantity $20 \log_{10} \mathcal{C}_{R,D}$ is minimal along the curve described by (16) as shown in the contour plot reported in Fig. 11(a).

Note that the residual added signal crosstalk $\mathcal{C}_{R,A}$ does not depend on K_3 . This can be easily understood because such a crosstalk, measured at the *Drop*-port, is the ratio between two signals which are traveling along the ring and coupled to the waveguide through the *Coupler*₃. For this reason, they are both multiplied by the same quantity $j\sqrt{K_3}$. Fig. 11(b) shows the contour plots of $20 \log_{10} (\mathcal{C}_{R,A})$ as a function of K_1 and K_2 . It is straightforward to see that $\mathcal{C}_{R,A}$ is negligible for either $K_1 = 0$ or $K_2 = 1$.

Additionally, we showed in Fig. 11(c) and (d) the $FWHM$ and ChR with respect to the coupling coefficients K_1 and K_2 . In order to have a sufficiently selective filter, K_1 and K_2 have to be smaller than 0.1. Ideally, we would like to have negligible crosstalk values and a small bandwidth for the same values of the coupling coefficients. However, the results displayed in Fig. 11 clearly show that we cannot optimize $\mathcal{C}_{R,D}$, $\mathcal{C}_{R,A}$, $FWHM$, and ChR at the same time. For example, for $K_1, K_2 \leq 0.1$, the crosstalks are larger than -20 dB, much larger than our constraint ($\mathcal{C}_{R,D}, \mathcal{C}_{R,A} < -40$ dB as we mentioned in Section I). Vice versa, for $K_1, K_2 > 0.1$ the 3 dB-bandwidth and ChR do not satisfy the constraints.

B. Two-Waveguide Switch

1) *Two-Waveguide Switch With a Single Ring*: For the simpler case shown in Fig. 5(a), the results are shown in Fig. 12, where the most important parameters have been plotted as a function of K_1 and K_2 . In order to guarantee a selective add/drop filter (small $FWHM$ and large ChR), the power coupling ratio K_1 and K_2 must be smaller than 0.15, which allows $\mathcal{C}_{R,D} \simeq -30$ dB. As explained in the introduction, smaller

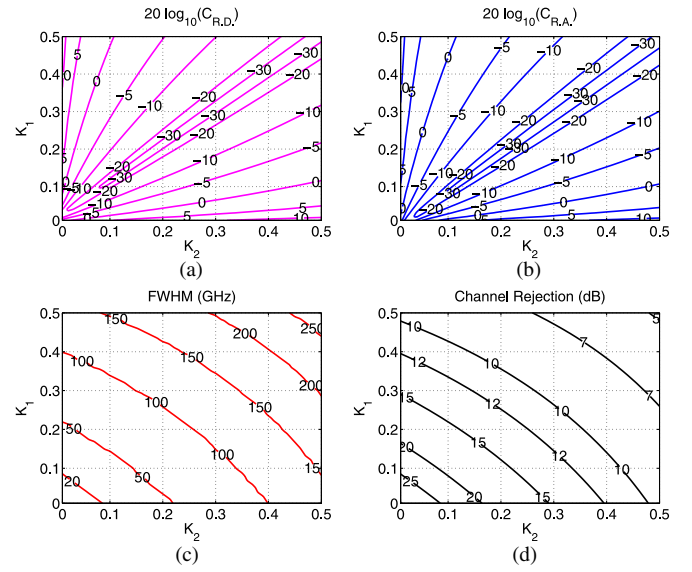


Fig. 12. (a) Contour plot of the residual dropped signal crosstalk $\mathcal{C}_{R,D}$. (b) Contour plot of the residual added signal crosstalk $\mathcal{C}_{R,A}$. (c) Contour plot of $FWHM$ for the single-ring switch. (d) Contour plot of ChR in dB.

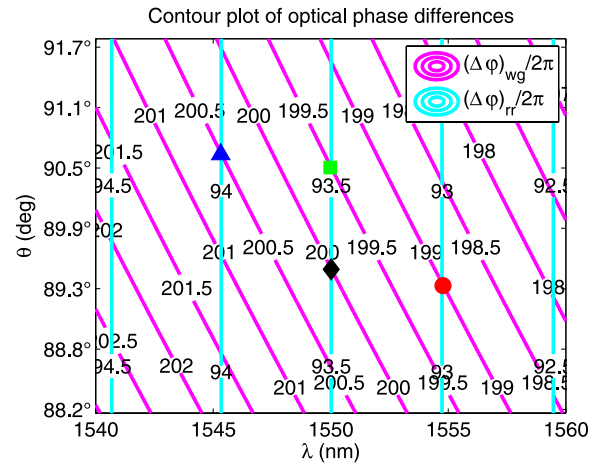


Fig. 13. Contour plot of $(\Delta\phi)_{wg}/2\pi$ and $(\Delta\phi)_{rr}/2\pi$ given in (11).

values are needed in order to guarantee low crosstalk at the drop-port.

2) *Two-Waveguide Switch With Two Rings*: Let us now focus on the more general case shown in Fig. 9. In order to investigate the behavior of the resonances of the rings and the figure-eight loop, we assumed $\lambda \in [1530, 1570]$ nm and we varied the angle between the two waveguides θ between 88.2° and 91.7° . As we mentioned in Section V, we have four possible resonances labeled as (α) – (δ) .

In Fig. 13, we have drawn the contour plot of both optical phase differences $(\Delta\phi)_{wg}/2\pi$ and $(\Delta\phi)_{rr}/2\pi$ given in (11). From that plot, we can easily identify the pair (λ, θ) which corresponds to one of the four possible cases: the symbol (\bullet) identifies the case (α) , when both the rings and figure-eight loop are resonating; the symbol (\blacktriangle) refers to the case (β) , when the rings are resonating and the figure-eight loop is completely out of resonance; finally, the last two symbols (\blacklozenge) and (\blacksquare) corre-

TABLE I
TWO-RING SWITCH: RESONANCE CASES

case	λ (nm)	θ (deg)	Ring resonance	Figure-eight loop resonance	Label in Fig. 13
α	1554.7	89.42	yes	yes	●
β	1545.3	90.67	yes	no	▲
γ	1550.0	89.56	no	yes	◆
δ	1550.0	90.52	no	no	■

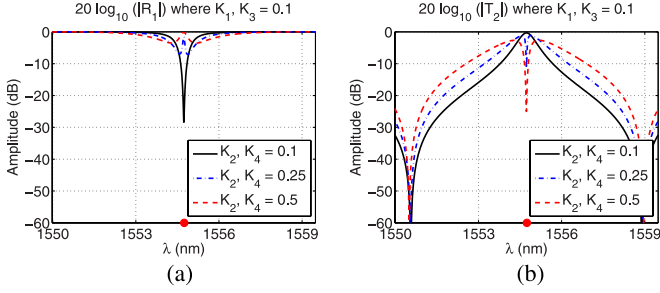


Fig. 14. Curves of coefficients R_1 and T_2 in dB when both the figure-eight-loop and the rings are resonating for $K_1 = K_3 = 0.1$ and $K_2 = K_4 = 0.1, 0.5, 0.9$. (a) Coefficient R_1 in dB. (b) Coefficient T_2 in dB.

spond to the case when the rings are completely out of resonance and the figure-eight loop is on resonance (γ) and completely out of resonance (δ), respectively. See Table I.

Note that in cases (γ) and (δ), the rings are completely out of resonance, so the added and dropped signals are negligible. We do not investigate those two cases because out of the scope of our analysis.

In order to analyze the behavior of $\mathcal{C}_{R.D.}$ and $\mathcal{C}_{R.A.}$ with respect to the power coupling constants K_1, K_2, K_3 , and K_4 , we have considered the two following cases which preserve the symmetry of the structure:

- 1) $K_1 = K_3, K_2 = K_4$;
- 2) $K_1 = K_4, K_2 = K_3$.

For a fixed wavelength and angle, the computations have been focused on the resonance cases (α) and (β).

Case (α), $K_1 = K_3, K_2 = K_4$: We introduce the coupling constants $K_{13} = K_1 = K_3$ and $K_{24} = K_2 = K_4$, and as a consequence $t_{13} = t_1 = t_3, k_{13} = k_1 = k_3, t_{24} = t_2 = t_4$, and $k_{24} = k_2 = k_4$, to have a more compact notation.

Fig. 14(a) and (b) shows the amplitude of coefficients R_1 and T_2 as a function of the wavelength for different values of the pair (K_{13}, K_{24}) . As it can be seen, when the ratio K_{13}/K_{24} is far from 1, T_2 shows a notch at the resonance wavelength λ_{res} . As a consequence, the light at λ_{res} tends to go to the *Add*-port instead of going to the *Drop*-port, i.e., R_1 is maximal, while T_2 becomes minimal. Vice versa, such behavior is less evident when K_{13} is close to K_{24} . As a result, this case has no interest for our application.

Let us note that this effect (“notch shape at the resonance”) is related to the “competitive resonances” in the switch: the two ring resonances and the figure-eight loop resonance. By varying the coupling coefficients K_i , we give prominence to one resonance condition with respect to the other one, causing this anomalous behavior.

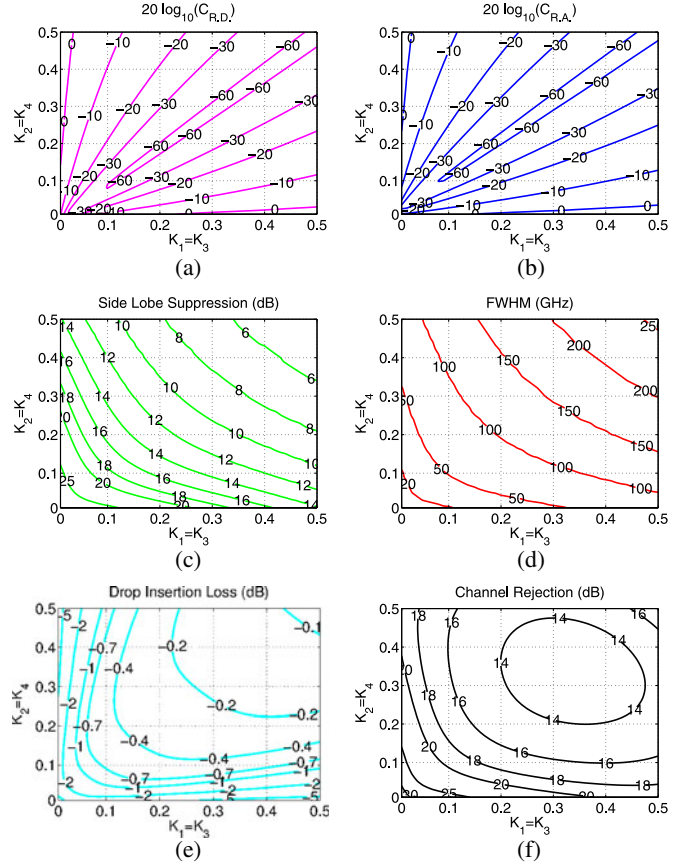


Fig. 15. Contour plots of $\mathcal{C}_{R.D.}$, $\mathcal{C}_{R.A.}$, SLS , $FWHM$, IL_d , and of ChR when $K_1 = K_3$ and $K_2 = K_4$ for the resonance case (β). (a) Contour plot of $\mathcal{C}_{R.D.}$ in dB. (b) Contour plot of $\mathcal{C}_{R.A.}$ in dB. (c) Contour plot of SLS in dB. (d) Contour plot of $FWHM$ in nm. (e) Contour plot of the IL_d in dB. (f) Contour plot of ChR in dB.

Case (β), $K_1 = K_3, K_2 = K_4$: In this case, using the coefficient t_{13}, t_{24}, k_{13} , and k_{24} previously defined, it can be shown that:

$$\mathcal{C}_{R.D.} = \frac{|p(t_{13} - t_{24}^* \tau)^2 (1 - t_{13}^* t_{24}^* \tau)|}{|k_{13} k_{24}^* \tau_i \eta + k_{13} k_{24}^* p^2 \tau_e (t_{13} - t_{24}^* \tau)(t_{24} - t_{13}^* \tau)|} \quad (17)$$

$$\mathcal{C}_{R.A.} = \frac{|p(t_{24} - t_{13}^* \tau)^2 (1 - t_{13}^* t_{24}^* \tau)|}{|k_{13}^* k_{24} \tau_i \eta + k_{13}^* k_{24} p^2 \tau_e (t_{13} - t_{24}^* \tau)(t_{24} - t_{13}^* \tau)|} \quad (18)$$

where $\eta = [(1 - t_{13}^* t_{24}^* \tau)(1 - t_{13}^* t_{24}^* \tau) - (|k_{13}| |k_{24}| p \tau_e)^2]$.

The residual dropped crosstalk $20 \log_{10}(\mathcal{C}_{R.D.})$ is minimal when the numerator of $\mathcal{C}_{R.D.}$ in (17) goes to zero, i.e., along the straight line $K_{13} = |\tau|^2 K_{24} + 1 - |\tau|^2$ on the (K_{13}, K_{24}) -plane, as shown in Fig. 15(a). Similarly, it can be seen that $20 \log_{10}(\mathcal{C}_{R.A.})$ is minimal when the numerator in (18) goes to zero, i.e., along the straight line $K_{13} = |\tau|^{-2} K_{24} + 1 - |\tau|^{-2}$, as shown in Fig. 15(b).

Additionally, we have also computed SLS , $FWHM$, IL_d , and ChR which are shown in Figs. 15(c)–(f), respectively. Those parameters have been computed referring to the

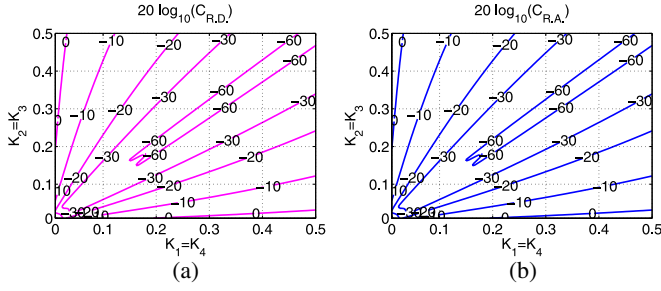


Fig. 16. Contour plots of $\mathcal{C}_{R.D.}$, $\mathcal{C}_{R.A.}$ when $K_1 = K_4$ and $K_2 = K_3$ in the resonance case (β). (a) Contour plot of $\mathcal{C}_{R.D.}$ in dB. (b) Contour plot of $\mathcal{C}_{R.A.}$ in dB.

coefficient T_2 , which has the following form

$$T_2 = \frac{k_{13}^* k_{24} \tau_i \eta + k_{13}^* k_{24} p^2 \tau_e (t_{13} - t_{24}^* \tau) (t_{24} - t_{13}^* \tau)}{(1 - t_{13}^* t_{24} \tau) \eta} \quad (19)$$

Considering the plots in Fig. 15, it is straightforward to identify a region on the (K_{13}, K_{24}) -plane where both $\mathcal{C}_{R.D.}$ and $\mathcal{C}_{R.A.}$ are small, the SLS is high and the filter is selective (small $FWHM$ and large ChR) with an acceptable IL_d value. For example, for $K_{13} = K_{24} = 0.1$, $\mathcal{C}_{R.D.} \simeq \mathcal{C}_{R.A.} \simeq -35$ dB, $SLS \simeq 18$ dB, $FWHM \simeq 0.4$ nm, $IL \simeq -0.7$ dB, and $ChR \simeq 19$ dB, which satisfy the constraints for several applications of practical interest.

Case (α), $K_1 = K_4$ and $K_2 = K_3$: As before, let us introduce the coupling constants $K_{14} = K_1 = K_4$ and $K_{23} = K_2 = K_3$, and as a consequence, $t_{14} = t_1 = t_4$, $k_{14} = k_1 = k_4$, $t_{23} = t_2 = t_3$, and $k_{23} = k_2 = k_3$. With such a notation, the transmission coefficient T_2 becomes

$$T_2 = \frac{k_{14}^* k_{23} \tau_i \xi + k_{14}^* k_{23} p^2 \tau_e (t_{14} - t_{23}^* \tau) (t_{23} - t_{14}^* \tau)}{(1 - t_{14}^* t_{23} \tau) \xi} \quad (20)$$

where $\xi = [(1 - t_{14}^* t_{23} \tau)(1 - t_{23}^* t_{14} \tau) - (k_{14} k_{23}^* p \tau_e)^2]$. Let us observe that (20) has the same form of (19) in the lossless case, when we replace K_{14} and K_{24} with K_{13} and K_{23} , as previously defined. As a consequence, this case is analogous to the resonance case (α) when $K_1 = K_3$ and $K_2 = K_4$, and it is not appealing for our purposes.

Case (β), $K_1 = K_4$ and $K_2 = K_3$: The residual dropped and added crosstalks take the following forms

$$\mathcal{C}_{R.D.} = \frac{|p(t_{14} - t_{23}^* \tau)(t_{23} - t_{14}^* \tau)(1 - t_{23}^* t_{14} \tau)|}{|k_{23}^* k_{14} \tau_i \xi + k_{14} k_{23}^* p^2 \tau_e (t_{23} - t_{14}^* \tau)(t_{14} - t_{23}^* \tau)|} \quad (21)$$

$$\mathcal{C}_{R.A.} = \frac{|p(t_{23} - t_{14}^* \tau)(t_{14} - t_{23}^* \tau)(1 - t_{14}^* t_{23} \tau)|}{|k_{14}^* k_{23} \tau_i \xi + k_{23}^* k_{14} p^2 \tau_e (t_{14} - t_{23}^* \tau)(t_{23} - t_{14}^* \tau)|} \quad (22)$$

In this case, $\mathcal{C}_{R.D.}$ is equal to $\mathcal{C}_{R.A.}$ and it is easy to see that they are negligible on the (K_{23}, K_{14}) -plane along the two following straight lines $K_{14} = 1 - (1 - K_{23})|\tau|^2$ and $K_{14} = 1 - (1 - K_{23})|\tau|^{-2}$. Figs. 16(a) and 16(b) show the contour plots of $\mathcal{C}_{R.D.}$ and $\mathcal{C}_{R.A.}$.

As we mentioned before, Eqs. (19) and (20) have the same form and, for this reason, SLS , $FWHM$, IL_d , and ChR are the same as in Fig. 15. Choosing small K_{13} and K_{24} values (e.g., $K_{13} = K_{24} = 0.1$), we can then design a suitable switching element for a ROADM.

At this point, it is worth to verify the hypothesis of optical linearity in the transfer function of the rings. Constructive interference at the coupler port ensures that circulating optical intensity is built up to a higher value than that one initially injected. As a consequence, a coherent buildup of intensity can lead to a dramatically enhanced nonlinear response and an optically induced phase change in the ring might occur [23]. To evaluate this phase change, let us notice that the power in the ring is

$$P_{\text{ring}} = \mathcal{B} P_{\text{in}} \quad (23)$$

where P_{in} is the power launched in the waveguide and \mathcal{B} is the buildup factor for an add-drop resonator [23]. Assuming the same values for all the coupling coefficients ($K = K_1 = K_2 = K_3 = K_4$), we have

$$P_{\text{ring}} \simeq \frac{1 - K}{K} P_{\text{in}}. \quad (24)$$

For $P_{\text{in}} = 5$ dBm ($\simeq 3$ mW) and $K = 0.1$, the power in the ring is $P_{\text{ring}} = 14.5$ dBm ($\simeq 28$ mW). Such a value, can induce a refractive index change Δn smaller than 10^{-4} [24], which corresponds to a resonance wavelength shift $\Delta \lambda$

$$\Delta \lambda = \lambda \frac{\Delta n}{n_g} = 38 \text{ pm} \quad (25)$$

this value corresponds to a frequency shift smaller than 5 GHz, which is acceptable within a 50 GHz bandwidth.

Considering the case (β), i.e. ring on resonance and figure-eight loop out of resonance, let us focus on the OFF state for the switching element under investigation. We have computed the ER and the IL_{bp} by shifting the transfer functions T_2 and R_1 with respect to the channel wavelength. To simplify our analysis, we assume that all the coupling coefficients have the same K value.

As it can be clearly seen from Fig. 17(a), the ER reaches its maximum for $K = 0.1$ and $\Delta \lambda \simeq 0.63$ nm. For those values, we have that $IL_{bp} < -0.1$ dB as shown in Fig. 17(b). Note that such a high value for the ER , which is larger than 35 dB, occurs because the maximum of the filter at ON-state [continuous line in Fig. 17(c)] matches the first zero-crossing of the switched ring transfer function [dashed line in Fig. 17(c)]. For the sake of completeness, we have also reported the through transfer function R_1 in Fig. 17(d), at ON state (continuous line) and OFF state (dashed line), respectively.

To complete our analysis, we have eventually computed the dispersion for the through and drop function, when $K = 0.1$. It is now useful to recall the definition of the group dispersion as

$$D = \frac{1}{2\pi c} \frac{\partial}{\partial \lambda} \left(\lambda^2 \frac{\partial \varphi}{\partial \lambda} \right) \quad (26)$$

where φ is the phase of the transfer function and c is the speed of light.

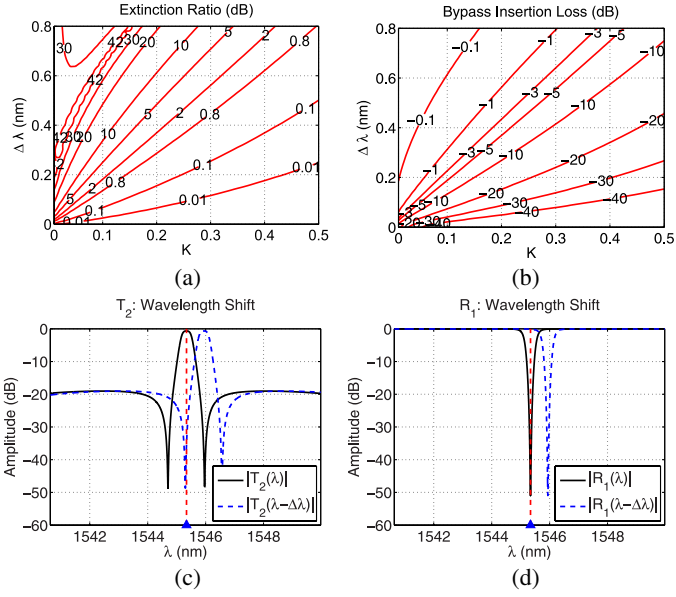


Fig. 17. OFF-state analysis. Contour plots of the ER and IL_{bp} as a function of $\Delta\lambda$ and K , and the spectra of T_2 and R_1 for $K = 0.1$. (a) Contour plot of the ER in dB. (b) Contour plot of the IL_{bp} in dB. (c) Drop transfer function. (d) Through transfer function.

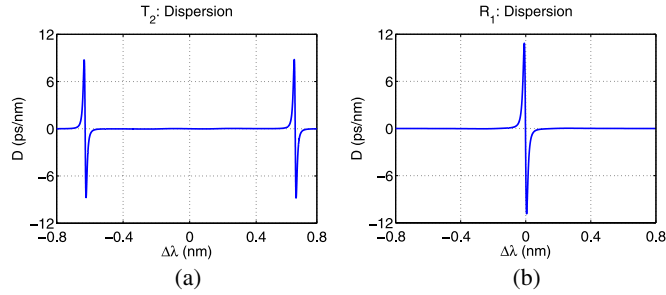


Fig. 18. Group dispersion of T_2 and R_1 for $K = 0.1$. (a) T_2 dispersion. (b) R_1 dispersion.

As we can see in Fig. 18, the dispersion is negligible when the ring is switched ON to drop a channel (center of the spectrum of T_2), and also when the ring acts as a bypass crosspoint (see the dispersion of $R_1(\lambda \pm \Delta\lambda)$, for $\Delta\lambda \simeq 0.63$ nm).

C. Sensitivity of Coherent Crosstalk With Respect to K_i

In this study, we have focused particular attention to minimize the two coherent crosstalk, i.e., $\mathcal{C}_{R,D}$ and $\mathcal{C}_{R,A}$, however, the device/device variability on the chip might seriously affect the performance of the TPA. For this reason, in this section, we explore the sensitivity of the above crosstalks with respect to the coupling coefficients K_i . As we have already seen, to satisfies the design constraint, we have chosen $K_1 = K_2 = K_3 = K_4 = 0.1$, it is then helpful to zoom Figs. 15(a), (b) and 16. As shown in Fig. 19, a variation of 15% of the coupling coefficients can still guarantee that $\mathcal{C}_{R,D}, \mathcal{C}_{R,A} < -35$ dB.

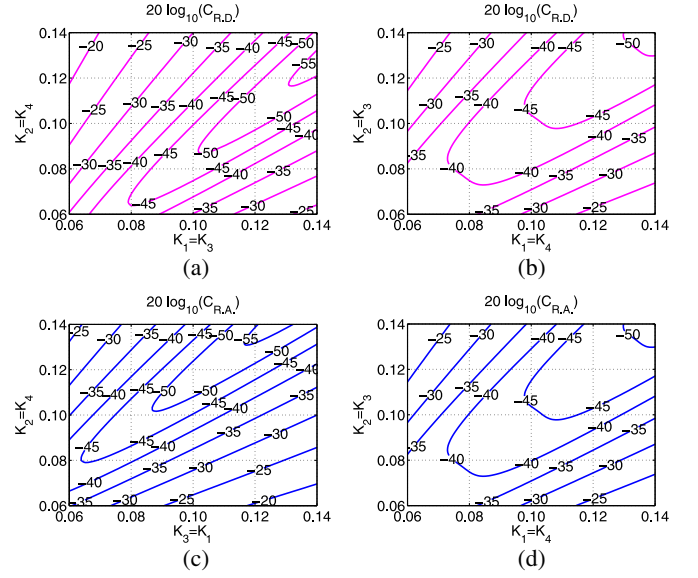


Fig. 19. Sensitivity of coherent crosstalk with respect to K_i . (a) Contour plot of $\mathcal{C}_{R,D}$ in dB. (b) Contour plot of $\mathcal{C}_{R,D}$ in dB. (c) Contour plot of $\mathcal{C}_{R,A}$ in dB. (d) Contour plot of $\mathcal{C}_{R,A}$ in dB.

VII. SOC TPA SUPPORTING HIGH SPEED TRANSMISSION AT 100 GB/S

In this section, the simulation results presented in Section VI are analyzed in order to verify the compliance of the integrated TPA design to the system specifications of CDC ROADM for metro network applications.

The TPA reference architecture is shown in Fig. 4. The number of directions N is typically up to 4 and the number of transponder ports M is typically 12. The transmitted WDM signals are typically noncoherent OOK modulated up to 10 Gbps and coherent DP-QPSK modulated at 40 Gbps and 100 Gbps, while the number of supported wavelengths is up to 48 in a 100 GHz wavelength grid.

To transmit 100 Gbps DP-QPSK signals without distortion, an optical 3 dB bandwidth of the switching elements larger than 50 GHz is needed, while the adjacent channel crosstalk for the dropped signal should be less than -30 dB. Considering an adjacent channel rejection of the integrated AWG larger than 15 dB, the ChR requirement of the microring switching elements should be higher than 15 dB. Note that the residual added signal crosstalk is the most harmful impairment due to the power level unbalance between the received signal and the locally added signal, which is assumed to be up to 20 dB. Because the two signals are at the same wavelength, no wavelength-selective block can be used to relax the requirements for this type of crosstalk, thus $\mathcal{C}_{R,A}$ should be lower than -40 dB. On the other hand, $\mathcal{C}_{R,D}$ is less critical since the power unbalance is favorable in this case. Concerning the incoherent noise, such a crosstalk must be smaller than -20 dB, which requests an $ER < -35$ dB.

From the results presented in this paper, it can be concluded that the microring switch configurations in Fig. 5(a) and (b) cannot fulfill the requirements of residual added and residual dropped crosstalk. Only the two-waveguide switch with two

rings can comply with the aforementioned system requirements, as shown in Fig. 15. With coupling coefficient values $K_1 = K_2 = K_3 = K_4$ of about 0.1, it is possible to achieve residual added and dropped crosstalk values lower than -40 dB, a 3 dB-bandwidth larger than 50 GHz, an adjacent channel rejection above 15 dB with an acceptable values of the insertion loss (< 1 dB) and SLS (> 20 dB).

Concerning the OFF state of the ring, for a 100 GHz-spaced WDM signal, the ring resonance can be tuned at most by 50 GHz (0.4 nm), which means that the ring is resonating at a wavelength located between two consecutive channels. As it can be seen from Fig. 17(a), assuming $K = 0.1$ and $\Delta\lambda \simeq 0.4$ nm, we have $ER \simeq 15$ dB. For such a small value, integrated tunable filters located before the receiver can preserve the quality of the signal by filtering out the incoherent noise. To perform a wide range of tunability, microring resonator filters based on the Vernier effect can be effectively used [25]. Another possible solution to achieve higher ER (> 35 dB) is considering larger wavelength shift, e.g. $\Delta\lambda \simeq 0.63$ nm for $K = 0.1$. It is worth noting that for such $\Delta\lambda$, the channel spacing must be larger than $2\Delta\lambda = 1.26$ nm ($\simeq 157.5$ GHz) to ensure a small incoherent crosstalk (< 20 dB). For this reason, the two-ring switch we have designed can be exploited in a TPA configuration in which interleavers [26] are used to separate odd and even channels that are then switched by microring matrices working with a channel separation of 200 GHz. Alternatively higher order filters (e.g., three coupled ring switches [27]) can be considered to achieve higher ER at each microring switch element of the matrix. Note that for this solution, a negligible group dispersion and a very small bypass insertion loss can be reached (< 0.1 dB). These features are very important when the switching element acts as a bypass crosspoint.

VIII. CONCLUSION

Microring-resonator-based switching elements are very attractive for the implementation of integrated optical switching subsystems used for interconnecting equipments in an optical transport node. A novel architecture of an integrated low cost SoC TPA based on microring resonators has been proposed and discussed. The proposed TPA is able to simultaneously add and drop channels in a CDC ROADM without requiring a dual device (one for add and one for drop functions), with the additional benefits of reducing cost and footprint. This specific functionality poses new requirements to crosstalk characteristics. In this paper, the transfer matrix method has been used to study the physical properties of single-ring and two-ring switches. For the latter switching element, the angle between the two waveguides has been introduced as a new degree of freedom. After validating the mathematical model, we have focused our attention on the residual dropped signal crosstalk and on the residual added signal crosstalk, fixing different resonance wavelengths and angles (for the two-ring switch). Eventually, the behavior of the switching elements has been studied with respect to the coupling coefficients.

The switching elements have been optimized in order to have low residual dropped signal crosstalk, low residual added signal

crosstalk, high side-lobe suppression, small FWHM bandwidth, high extinction ratio and a sufficiently low insertion losses. Simulation results clearly show how competitive resonances (between the rings and amongst rings and figure-eight loop) might seriously affect the performance of the switch. In this study, we pointed out that the two-ring switch is more attractive, allowing to minimize both the dropped and residual crosstalks, showing high out of band rejection and side-lobe suppression for reasonable values of the coupling coefficients. The suitability of the proposed TPA in switching 100G DP-QPSK signals in a CDC-ROADM for metropolitan networks has been discussed. Configurations and design parameters of the microring switching elements have been validated to achieve the best tradeoff between channel selectivity and residual added and residual dropped signal crosstalk.

ACKNOWLEDGMENT

The authors would like to thank C. Oton for the useful discussion and the anonymous reviewers for the suggestions.

REFERENCES

- [1] B. Collings, "New devices enabling software-defined optical networks," *IEEE Commun. Mag.*, vol. 51, no. 3, pp. 66–71, Mar. 2013.
- [2] N. Andrioli, L. Valcarengi, and P. Castoldi, "Impact of node switching capabilities on the performance of wavelength routed networks," *Eur. Trans. Telecommun.*, vol. 17, no. 1, pp. 77–91, 2006.
- [3] R. Jensen, A. Lord, and N. Parsons, "Colourless, directionless, contentionless ROADM architecture using low-loss optical matrix switches," presented at the 36th Eur. Conf. Exhib. Opt. Commun., Turin, Italy, Sep. 19–23, 2010, Paper Mo.2.D.2.
- [4] P. Colbourne and B. Collings, "ROADM switching technologies," presented at the Opt. Fiber Commun. Conf. Expo., Los Angeles, CA, USA, Mar. 6–10, 2011, Paper OTuD1.
- [5] S. Gringeri, B. Basch, V. Shukla, R. Egorov, and T. J. Xia, "Flexible architectures for optical transport nodes and networks," *IEEE Commun. Mag.*, vol. 48, no. 7, pp. 40–50, Jul. 2010.
- [6] T. Watanabe, K. Suzuki, T. Goh, K. Hattori, A. Mori, T. Takahashi, T. Sakamoto, K. Morita, S. Sohma, and S. Kamei, "Compact PLC-based transponder aggregator for colorless and directionless ROADM," presented at the Opt. Fiber Commun. Conf. Expo., May 6–10, 2011, Los Angeles, CA, USA, Paper OTuD3.
- [7] T. Hino, H. Takeshita, M. Sakauchi, K. Ishii, J. Kurumida, S. Namiki, S. Takahashi, S. Nakamura, and A. Tajima, "Silicon photonics based transponder aggregator for next generation ROADM systems," presented at the Eur. Conf. Exhib. Opt. Commun., Amsterdam, The Netherlands, Sep. 16–20, 2012, Paper Tu.3A.5.
- [8] M. R. Watts, W. A. Zortman, D. C. Trotter, G. N. Nielson, D. L. Luck, and R. W. Young, "Adiabatic resonant microrings (ARMs) with directly integrated thermal microphotonic," presented at the Conf. Lasers Electro-Opt./Quant. Electron. Laser Sci. Conf., OSA Tech. Digest (CD), Baltimore, MD, USA, Jun. 2009, Paper CPDB10.
- [9] P. Dong, W. Qian, H. Liang, R. Shafiqhi, N.-N. Feng, D. Feng, X. Zheng, A. V. Krishnamoorthy, and M. Asghari, "Low power and compact reconfigurable multiplexing devices based on silicon microring resonators," *Opt. Expr.*, vol. 18, no. 10, pp. 9852–9858, 2010.
- [10] B. E. Little, S. T. Chu, W. Pan, and Y. Kokubun, "Microring resonator arrays for VLSI photonics," *IEEE Photon. Technol. Lett.*, vol. 12, no. 3, pp. 323–325, Mar. 2000.
- [11] S.-J. Chang, C.-Y. Ni, Z. Wang, and Y.-J. Chen, "A compact and low power consumption optical switch based on microrings," *IEEE Photon. Technol. Lett.*, vol. 20, no. 12, pp. 1021–1023, Jun. 15, 2008.
- [12] A. W. Poon, L. Xianshu, X. Fang, and C. Hui, "Cascaded microresonator-based matrix switch for silicon on-chip optical interconnection," *Proc. IEEE*, vol. 97, no. 7, pp. 1216–1238, Jul. 2009.
- [13] W. Bogaerts, P. Dumon, D. Van Thourhout, and R. Baets, "Low-loss, low-cross-talk crossings for silicon-on-insulator nanophotonic waveguides," *Opt. Lett.*, vol. 32, no. 19, pp. 2801–2803, Oct. 2007.

- [14] Y. Zhang, S. Yang, A. E.-J. Lim, G.-Q. Lo, C. Galland, T. Baehr Jones, and M. Hochberg, "A CMOS-compatible, low-loss, and low-crosstalk silicon waveguide crossing," *IEEE Photon. Technol. Lett.*, vol. 25, no. 5, pp. 422–425, Mar. 2013.
- [15] E. Marchena, T. Creazzo, S. B. Krasulick, P. Yu, D. Van Orden, J. Y. Spann, C. C. Blivin, J. M. Dallesasse, P. Varangis, R. J. Stone, and A. Mizrahi, "Integrated tunable CMOS laser for Si photonics," presented at the Opt. Fiber Commun. Conf./Nat. Fiber Opt. Eng. Conf., Anaheim, CA, USA, 2013, Paper PDP5C.7.
- [16] B. R. Koch, E. J. Norberg, B. Kim, J. Hutchinson, J. Shin, G. Fish, and A. Fang, "Integrated silicon photonic laser sources for telecom and datacom," presented at the Opt. Fiber Commun. Conf./Nat. Fiber Opt. Eng. Conf., Anaheim, CA, USA, 2013, Paper PDP5C.8.
- [17] A. Yariv, "Universal relations for coupling of optical power between microresonators and dielectric waveguides," *Electron. Lett.*, vol. 36, no. 4, pp. 321–322, Feb. 17, 2000.
- [18] J. Capmany, P. Muñoz, J. D. Domenech, and M. A. Muriel, "Apodized coupled resonator waveguides," *Opt. Expr.*, vol. 15, no. 16, pp. 10196–10206, Aug. 6, 2007.
- [19] J. Jin, *The Finite Element Method in Electro-Magnetics*, 2nd ed. New York, NY, USA: Wiley, 2002.
- [20] A. Konrad, "High-order triangular finite elements for the electromagnetic waves in anisotropic media," *IEEE Trans. Microw. Theory Tech.*, vol. 25, no. 5, pp. 353–360, May 1977.
- [21] S. K. Selvaraja, P. Jaenen, W. Bogaerts, D. V. Thourhout, P. Dumon, and R. Baets, "Fabrication of photonic wire and crystal circuits in silicon-on-insulator using 193 nm optical lithography," *J. Lightwave Technol.*, vol. 27, no. 18, pp. 4076–4083, Sep. 15, 2009.
- [22] S. Feng, T. Lei, H. Chen, H. Cai, X. Luo, and A. W. Poon, "Silicon photonics: From a microresonator perspective," *Laser Photon. Rev.*, vol. 6, no. 2, pp. 145–177, Apr. 2012.
- [23] J. Heebner, R. Grover, and T. A. Ibrahim, *Optical Microresonators, Theory, Fabrication and Applications*. London, U.K.: Springer-Verlag, 2008.
- [24] G. R. A. Priem, P. Dumon, W. Bogaerts, D. Van Thourhout, G. Morthier, and R. Baets, "Optical bistability and pulsating behaviour in Silicon-On-Insulator ring resonator structures," *Opt. Expr.*, vol. 13, no. 23, pp. 9623–9628, 2005.
- [25] M. S. Rasras, D. M. Gill, M. P. Earnshaw, C. R. Doerr, J. S. Weiner, C. A. Bolle, and Y.-K. Chen, "CMOS silicon receiver integrated with Ge detector and reconfigurable optical filter," *IEEE Photon. Technol. Lett.*, vol. 22, no. 2, pp. 112–114, Jan. 2010.
- [26] F. Horst, W. M. J. Green, S. Assefa, S. M. Shank, Y. A. Vlasov, and B. J. Offrein, "Cascaded Mach-Zehnder wavelength filters in silicon photonics for low loss and flat pass-band WDM (de-)multiplexing," *Opt. Expr.*, vol. 21, no. 10, pp. 11652–11658, 2013.
- [27] F. Xia, M. Rooks, L. Sekaric, and Y. Vlasov, "Ultra-compact high order ring resonator filters using submicron silicon photonic wires for on-chip optical interconnects," *Opt. Expr.*, vol. 15, no. 19, pp. 11934–11941, 2007.

Paolo Pintus (S'10–M'11) was born in Cagliari, Italy, in 1983. He received the Bachelor's degree (with Hons.) in electronic engineering and the Master's degree (with Hons.) both from the University of the Studies of Cagliari, Cagliari, in 2005 and 2007, respectively, and the Ph.D. degree in innovative technologies of ICT and robotics from the Scuola Superiore di Studi Universitari e Perfezionamento Sant'Anna, Pisa, Italy, in 2012.

He was a Visiting Student (Leonardo da Vinci program) at the Crisanti Lab, Department of Biological Sciences, Imperial College of London, London, U.K. He was a Visiting Researcher at Optoelectronics Research Group, University of California Santa Barbara, Santa Barbara, CA, USA. He is currently a Research Fellow at the Scuola Superiore di Studi Universitari e Perfezionamento Sant'Anna, Pisa, Italy. His research interests include silicon photonics, integrated optics, and numerical method for electromagnetism.

Pietro Contu was born in Cagliari, Italy, in 1982. He received the Bachelor's degree (with Hons.) in physics, the Master's degree (with Hons.) in nuclear physics, and the Ph.D. degree in mathematics and computer science, all from the University of the Studies of Cagliari, Cagliari, in 2004, 2007, and 2011, respectively.

He is currently a Research Fellow at the Scuola Superiore di Studi Universitari e Perfezionamento Sant'Anna, Pisa, Italy. His research interests include photonic crystals, integrated optics, and numerical method for electromagnetism.

Nicola Andriolli received the Laurea degree in telecommunications engineering from the University of Pisa, Pisa, Italy, in 2002, and the Dipl. and Ph.D. degrees from Scuola Superiore Sant'Anna, Pisa, in 2003 and 2006, respectively.

He was a Visiting Student in the Department of Communications, Optics and Materials, Technical University of Denmark, Copenhagen, Denmark. He was a Guest Researcher at the National Institute of Information and Communications Technology, Tokyo, Japan. He is currently an Assistant Professor at Scuola Superiore Sant'Anna. His research interests include the design and the performance analysis of optical circuit-switched and packet-switched networks and nodes, optical interconnection network architectures and scheduling, as well as optical integration technologies.

Antonio D'Errico was born in San Severo, Italy, in 1974. He received the Ph.D. degree (*cum laude*) in telecommunication engineering from the Scuola Superiore Sant'Anna, Pisa, Italy, in 2008.

He was a Researcher at the Consorzio Nazionale Interuniversitario per le Telecomunicazioni (CNIT), Pisa, from 2008 to 2009. He is currently with Ericsson Research, Pisa, as a Senior Researcher. He is the author or coauthor of more than 65 papers published in high-impact-factor international journals, conference digests, and patents. He is on the board of reviewers for a number of international journals fields of optical communications and photonics. His research interests include optical telecommunication systems and advanced solutions for the optical transport networks.

Fabrizio Di Pasquale (M'04) was born in Italy in 1963. He received the Graduate degree in electronic engineering from University of Bologna, Bologna, Italy, in 1989 and the Ph.D. degree in information technology from University of Parma, Parma, Italy, in 1993.

From 1993 to 1998, he was in the Department of Electrical and Electronic Engineering, University College London, London, U.K., as a Research Fellow, working on optical amplifiers, WDM optical communication systems, and liquid crystal displays. After two years with Pirelli Cavi e Sistemi and two years with Cisco Photonics Italy, he is currently an Associate Professor in telecommunications at the Scuola Superiore Sant'Anna, Pisa, Italy. He has filed 20 international patents and he is the author and co-author of over than 150 scientific journals and conference papers in the areas of optical amplifiers, optical communications systems, liquid crystal displays, and distributed optical fiber sensors. His current research interests include optical amplifiers, WDM transmission systems and networks, and optical fiber sensors.

Dr. Di Pasquale is on the Board of Reviewers of the IEEE PHOTONICS TECHNOLOGY LETTERS, the IEEE/OSA JOURNAL OF LIGHTWAVE TECHNOLOGY, the *Optics Communications*, the *Optics Express*, and the *Optics Letters*.

Francesco Testa received the Laurea degree in electronic engineering (*summa cum laude*) from the University of Rome, Rome, Italy, in 1980.

In 1982, he was granted a scholarship from Fondazione Ugo Bordoni-Roma working on Integrated optics. He started working at Alcatel-Face Italy on the research of coherent optical systems in 1985. He joined Ericsson in 1991, where he worked on the first demonstrations of WDM systems in the framework of the European projects RACE and ACTS. He was later involved in the hardware design and development of SDH, DECT, local multipoint distribution system (LMDS), and GSM products. In 2008 he has been again engaged in research activity on architectures and technologies for next generation optical transport networks, including high-capacity switching and high-speed transmission. He is currently leading a team working on the development of photonic integrated devices. He coauthored many papers and patents in the field of optical and radio communications.